



PAPER • OPEN ACCESS

Breaking the mass law for broadband sound insulation through strongly nonlinear interactions

To cite this article: Xin Fang *et al* 2023 *New J. Phys.* **25** 093010

View the [article online](#) for updates and enhancements.

You may also like

- [Low frequency sound insulation performance of membrane-type acoustic metamaterial with eccentric mass block](#)
Tong Cai, Shuang Huang, Hui Guo et al.
- [Multifunctional acoustic metamaterial for air ventilation, broadband sound insulation and switchable transmission](#)
Zhenqian Xiao, Penglin Gao, Xiao He et al.
- [Effect of tufting technique on sound insulation of multi-layer glass woven fabrics](#)
Hao Shen, Yong Yang, Peng Wang et al.



**PAPER**

Breaking the mass law for broadband sound insulation through strongly nonlinear interactions

OPEN ACCESS**RECEIVED**
25 June 2023**REVISED**
21 August 2023**ACCEPTED FOR PUBLICATION**
24 August 2023**PUBLISHED**
6 September 2023

Original content from
this work may be used
under the terms of the
[Creative Commons
Attribution 4.0 licence](#).

Any further distribution
of this work must
maintain attribution to
the author(s) and the title
of the work, journal
citation and DOI.

Xin Fang^{1,*} , Tao Li¹, Bin Hu¹, Miao Yu¹, Peng Sheng¹, Jihong Wen¹ and Li Cheng^{2,*} ¹ College of Intelligent Science, National University of Defense Technology, Changsha, Hunan 410073, People's Republic of China² Department of Mechanical Engineering, Hong Kong Polytechnic University, Hong Kong, People's Republic of China

* Authors to whom any correspondence should be addressed.

E-mail: xinfangdr@sina.com and li.cheng@polyu.edu.hk**Keywords:** sound insulation, nonlinear, broadband, mass law, metamaterial**Abstract**

Sound transmission through panels is governed by the well-known mass law in the mid-frequency range. This paper reveals a possibility of breaking this density-dominant law through strongly nonlinear interaction, while broadening the bandwidth for effective sound insulation. For this purpose, a basic model is established, and corresponding exact analytical methods for bifurcation and stability analyses are proposed. Influences of four typical types of nonlinear interactions on the wave insulation are analytically and numerically investigated. We find that, by introducing strongly nonlinear interactions at appropriate locations, the nonlinear model can not only break the barrier imposed by the mass law, but also entails broadband sound insulation by 2–3 times relative to the optimal linear model. Meanwhile, the sound insulation valley due to the coincident effects can also be eliminated. With bifurcation and effective mass, we clarify that the enhanced wave insulation of the strongly nonlinear models arises from the broader band of super mass induced by strongly nonlinear local resonances, which depends on the bifurcation of periodic solutions. The proposed models and the findings provide a solid basis and new possibilities for wave insulation in complex nonlinear structures and nonlinear acoustic metamaterials.

1. Introduction

Insulation of low-frequency and broadband sound and elastic wave is of great significance for a wide range of applications, such as protecting buildings from earthquake waves, reducing noise of airplane cabin (insulating fluid and aeroengine noise) [1, 2], or conceiving various wave manipulation devices. It is well known that sound insulation of a monolayer plate/wall generally follow the mass-density law in the mid-frequency range beyond the stiffness-dominant region and before the coincidence frequency [3], i.e. the transmission loss $T_L = 20\log(\omega M/2\rho c)$, where ω denotes the angle frequency; M the surface density of the wall; ρ and c the medium density and sound speed, respectively. This law stipulates that a heavy panel is needed to achieve good sound insulation. More specifically, improving the sound insulation by 6 dB requires doubling the surface density of the panel. For a finite plate with boundary, the insulation of very low-frequency sound depends on the structural stiffness. Between the stiffness-dominant band and the density-dominant band, a coincidence frequency appears, where the transmission loss becomes zero. It is an eternal pursuit to find ways to effectively insulate low-frequency and broadband sound with small weight cost. Many linear ways have been attempted, but the challenge remains [4].

From a different perspective and analogous to the mechanical nonlinear energy sink (NES) [5, 6], Bellet *et al* [7] proposed a nonlinear acoustic absorber that can effectively dissipate the resonant or transient response of an acoustic cavity or tube. Such nonlinear acoustic absorber can be made of a viscoelastic membrane or loudspeaker attaching to an orifice of a cavity [7–12]. The problem can be simplified to a two-degrees-of-freedom (2DoF) nonlinear mechanical system [8]. However, the way to insulate acoustic waves (instead of absorbing waves) using NES has not been clearly understood.

A method that can eventually overcome the density-dominant mass law for sound insulation is using acoustic metamaterials, a research field which attracted great attention in the past 20 years [13–17]. Acoustic metamaterial plates, with periodically attached resonators on a plate [18], can induce negative effective density in a locally resonant band, which can eventually break the mass law of a wall/plate [19–23]. This can be made possible by using mechanical resonators or inductance-capacitance (LC) electric circuits [24]. However, these attempts were made based on linear dynamics, i.e. linear acoustic metamaterials (LAMs). In a LAM, the bandwidth of wave insulation peak is narrowband in nature, and an insulation valley (with T_L tending to 0) generally appears near the peak [18]. This valley may jeopardize the benefit of the metamaterial design.

Recently, nonlinear acoustic metamaterials (NAMs) [25–27], with embedded nonlinear local resonators, have attracted increasing attention owing to their outstanding features that are absent in their linear counterparts. NAMs' bandgaps are amplitude-dependent [25, 28–33], which is essentially dominated by the band degeneration process [34]. NAM [35, 36] can induce nonreciprocal wave transmission [37], i.e. the diode behavior [38]. NAMs with strong nonlinearity can induce self-broadening bandgaps that can be eight times broader than the linear metamaterial with the same attached mass ratio [39]. NAMs can also offer numerous interesting properties including harmonic generation [29, 31, 40], frequency down-conversion [41] and wave self-interaction [42] etc. Moreover, enabled by the chaotic band mechanism, NAMs can achieve ultralow-frequency and ultrabroad band (double-ultra) vibration reduction and sound radiation attenuation [43, 44]. The bandwidth can be two orders of magnitude higher than the linear bandgaps. Recently, this benefit was demonstrated on a lightweight sandwich plate with light-weighted and strongly nonlinear resonators [45]. In summary, both amplitude-dependent bandgap and diode are 'wave insulation' behaviors. Generally, generating these behaviors requires more than five layers of unit cells, although the possibility of realizing diode behavior within three layers was demonstrated [38]. However, the potentials and mechanisms of NAMs to achieve enhanced sound wave insulation as compared with a monolayer plate, have not been studied.

This issue is investigated in this paper by examining the basic physical model of a plate/wall immersed in fluid. The objective is to explore system nonlinearity to break the mass law governing the acoustic wave insulation while achieving broadened sound insulation bandwidth. To this end, we establish a 1D chain that can represent the basic model of 'a monolayer wall/panel immersed in fluid'. Two coupled oscillators are attached to the wall. This model can represent NESs and a nonlinear metamaterial unit cell. Influences of nonlinear boundary and nonlinear coupling between the resonators on wave insulation are comprehensively studied with numerical and analytical methods. We find that, using proper strongly nonlinear interactions can not only break the mass law, but also broaden the bandwidth for great wave insulation by more than 2–3 times relative to the optimal linear model. Physical mechanisms underpinning this superior property are clarified with the effective mass/density concepts in metamaterials.

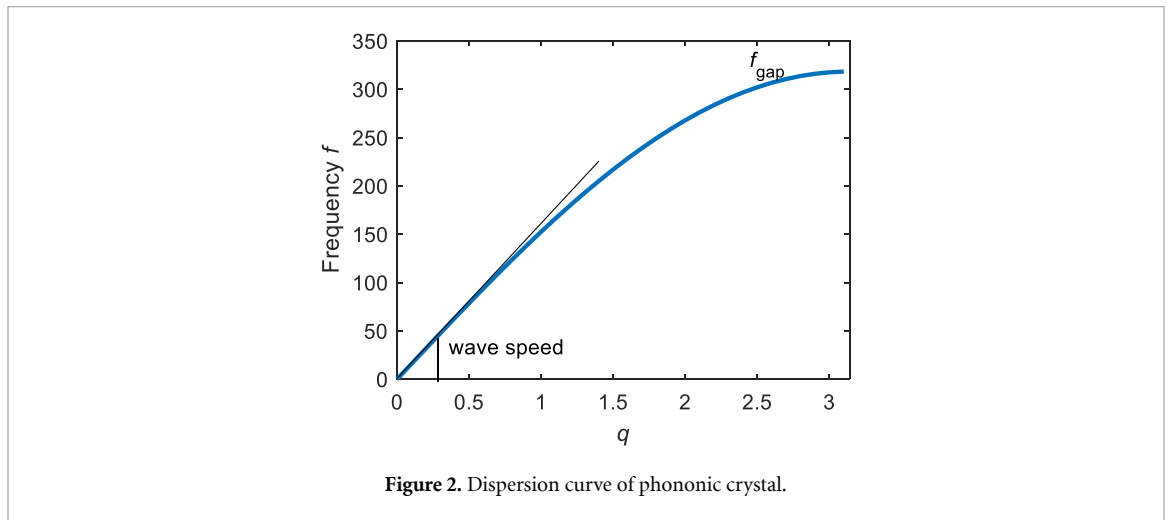
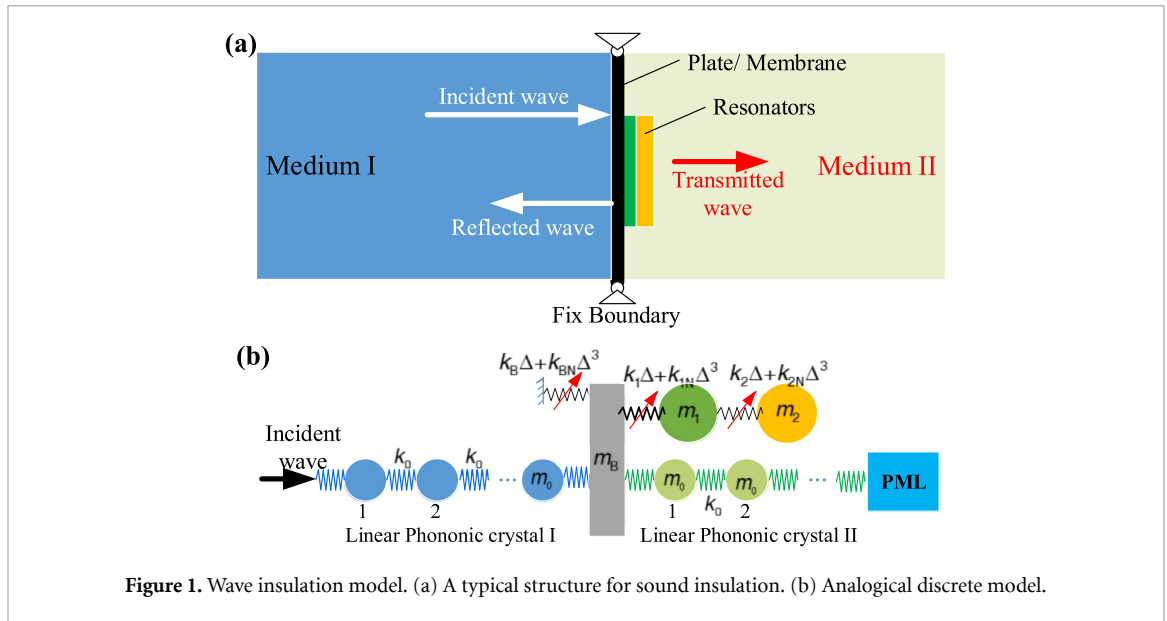
2. Model and methods

2.1. Model

Figure 1(a) shows a plate (membrane or wall) with surface-mounted local resonators. The plate is immersed in acoustic media I and II. While sound insulation of LAMs can be well apprehended with frequency-domain finite element methods, the nonlinear system under investigation requires special treatment for analysis. As shown in figure 1(b), to find nonlinear ways that may overcome the 'narrow band' and 'concomitant insulation valley' disadvantages of acoustic metamaterial, we establish an analogical discrete model that can not only reflect the essential wave insulation properties of the nonlinear systems, but also can be efficiently solved in time domain as well as with approximate analytical solutions. The model consists of a linear phononic crystal I, a 3DoF nonlinear system, another linear phononic crystal II and a perfect match layer (PML). Phononic crystals I and II can simulate the low-frequency wave propagation (much lower than the bandgap frequency) in the homogenous media I and II, respectively (as further explained below). The nonlinear system, inserted between phononic crystals I and II, consists of a primary mass m_B , two coupled local resonators m_1 and m_2 , and a boundary spring. The primary mass m_B models the wall for wave/sound insulation, and the spring k_B models the influence of the boundary stiffness. Therefore, this model can represent either a NES or a metamaterial design, because one generally considers a periodic unit cell of metamaterial.

The phononic crystals I and II comprise periodic mass, m_0 , and linear springs, k_0 . The motion equation of the n th cell writes:

$$m_0 \ddot{u}_n = k_0(u_{n+1} - u_n) - k_0(u_n - u_{n-1}), \quad (1)$$



where u_n denotes the displacement of the n th m_0 . Replacing k_0 with k_{0I} and k_{0II} distinguishes crystals I and II. By introducing the Bloch theorem, we obtain the dispersion equation (see figure 2) of this mono-atomic chain as:

$$2k_0(1 - \cos q) = \omega^2 m_0, \tag{2}$$

in which q symbolizes the wave vector and $\omega = 2\pi f$ denotes the angular frequency. At $q = \pi$, one gets the initial frequency of bandgap of the chain, $f_{\text{gap}} = \sqrt{k_0/m_0}/\pi$.

The wave speed, $c = d\omega/dq$, can be solved by equation (2). At $q = 0$, long-wave speed is $c_0 = \sqrt{k_0/m_0}$. For the low-frequency wave of frequency $f \ll f_{\text{gap}}$, the wave speed decreases only slightly with respect to c_0 and can be considered constant. Therefore, at frequencies much lower than the bandgap frequency, phononic crystals I and II can simulate low-frequency wave propagation with constant wave speed in continuous media I and II, respectively. In this case, equation (1) can be regarded as a difference equation. Furthermore, u is a function of propagation distance, x , and time, t . Therefore, equation (1) can be rewritten as a partial differential equation:

$$\frac{\partial^2 u}{\partial t^2} = c_0^2 \frac{\partial^2 u}{\partial x^2} \tag{3}$$

which is the linear sound equation in a homogeneous medium like air. Due to dispersive effects, note that the above equivalent process between equations (1) and (3) is valid only for $f \ll f_{\text{gap}}$. In the present case, if we

define a limiting frequency f_{eq} in order to comply with $c(f_{\text{eq}}) = 0.8c_0$, the derivation $d\omega/dq$ yields $f_{\text{eq}} \approx 0.61f_{\text{gap}}$.

In the 3DoF nonlinear system, the primary mass m_B connects to the foundation through the nonlinear spring $k_B u_B + k_{\text{BN}} u_B^3$, where k_B and k_{BN} denote the linear and nonlinear stiffness coefficients, respectively; and u_B denotes the displacement of m_B . m_1 is coupled to m_B through the nonlinear force $k_1(y - u_B) + k_{1\text{N}}(y - u_B)^3$, and m_2 interacts with m_1 by the nonlinear force $k_2(z - y) + k_{2\text{N}}(z - y)^3$, where k_i and $k_{i\text{N}}$ denote the linear and nonlinear stiffness coefficient, respectively, $i = 1, 2$; and y and z symbolize the displacement of m_1 and m_2 , respectively. Therefore, m_2 is indirectly coupled to m_B . Only the typical cubic nonlinearity is considered here. The equations of motion read:

$$\begin{cases} m_B \ddot{u}_B = k_1(y - u_B) + k_{1\text{N}}(y - u_B)^3 + F \\ m_1 \ddot{y} = -k_1(y - u_B) - k_{1\text{N}}(y - u_B)^3 + k_2(z - y) + k_{2\text{N}}(z - y)^3, \\ m_2 \ddot{z} = -k_2(z - y) - k_{2\text{N}}(z - y)^3 \end{cases}, \quad (4)$$

in which, F denotes the total force from the three boundaries. In the numerical model,

$$F = -k_B u_B - k_{\text{BN}} u_B^3 - k_{0\text{I}}(u_{\text{LN}} - u_B) + k_{0\text{II}}(u_{\text{R1}} - u_B), \quad (5)$$

where u_{LN} is the displacement of the last m_0 in crystal I; u_{R1} is the displacement of the first m_0 of crystal II. An incident wave is emitted from the left terminal of the chain I. Let us define the incident, reflected and transmitted wave fields as $u_i(x, t)$, $u_r(x, t)$, $u_t(x, t)$, respectively. For a continuous system, taking equation (5) as a difference equation at the boundary $x = 0$ yields:

$$F = -k_B u_B - k_{\text{BN}} u_B^3 - k_{0\text{I}} \left. \frac{\partial(u_i + u_r)}{\partial x} \right|_{x=0} + k_{0\text{II}} \left. \frac{\partial u_t}{\partial x} \right|_{x=0}. \quad (6)$$

This equation describes the interaction between the wave field and the wall structure.

The following parameters are used in the subsequent numerical analyses: $m_0 = 0.001$ g, $c_0 = 1000$ s⁻¹, $m_B = 0.004$ g, $k_B = m_B(40\pi)^2$, $m_1 = m_2 = 0.002$ g; $\omega_1 = 200\pi$, $\omega_2 = 100\pi$. Moreover, $f_{\text{gap}} = 318$ Hz and $f_{\text{eq}} \approx 195$ Hz. The incident wave amplitude is $u_{\text{ia}} = 40$ μm . Nonlinearity is tuned by changing the nonlinear stiffness coefficients. We specify $k_1 > k_2$ to ensure effective energy transfer from m_B to m_2 .

2.2. Numerical methods

Wave propagation in this chain can be solved by time-domain numerical integral method, but we must model the non-reflection boundary. For that, the length of phononic crystal I should be longer than $c_0 \times T$, where T is the total time length of the incident wave packet. Here, phononic crystal I consists of 180 cells, and crystal II has 60 cells. Crystal II can be short because an optimized perfect match layer (PML) is connected to it. The PML consists of 120 periodic cells with damping. The motion equation of PML oscillators is

$$m_0 \ddot{u}_n = k_{0\text{II}}(u_{n+1} + u_{n-1} - 2u_n) + d_0 k_{0\text{II}}(\dot{u}_{n+1} + \dot{u}_{n-1} - 2\dot{u}_n).$$

Here, the damping coefficient $d_0 = 0.0015$.

Moreover, to eliminate the influence of the boundary reflection and to distinguish the incident wave and reflection wave in crystal I, we use a ten-period sinusoidal wave packet as the input signal. The numerical integral time is 0.8 s. Typical wave forms are shown in figure 3, in which different wave components can be clearly identified. Furthermore, we extract all peaks of the transmitted wave packet, and use their average value u_{tav} to calculate the transmission loss $T_L = 20 \log_{10}(u_{\text{ia}}/u_{\text{tav}})$.

2.3. Analytical method for linear model

For linear model, when $k_{\text{BN}} = k_{1\text{N}} = k_{2\text{N}} = 0$, we adopt the effective mass of the metacell to calculate the wave insulation. In this case, taking force F in equation (4) as an unknown variable, the effective mass of the linear model reads:

$$m_{\text{eff,L}} = \frac{F}{\ddot{u}_B} = m_B + \frac{k_2 \omega_1^2 + k_1(\omega_2^2 - \omega^2)}{(\omega_1^2 - \omega^2)(\omega_2^2 - \omega^2) - \omega^2 k_2 / m_1}, \quad (7)$$

where $\omega_i^2 = k_i / m_i$, $i = 1, 2$. The total mass $m_t = m_B + m_1 + m_2$. Local resonators will not only present the negative mass $m_{\text{eff,L}} < 0$, but also the unusual bands for $|m_{\text{eff,L}}/m_B| > 1$ or $|m_{\text{eff,L}}/m_t| > 1$, which are defined as the ‘super mass’ relative to the primary mass m_B and the total mass m_t , respectively. Super mass is paramount to wave insulation.

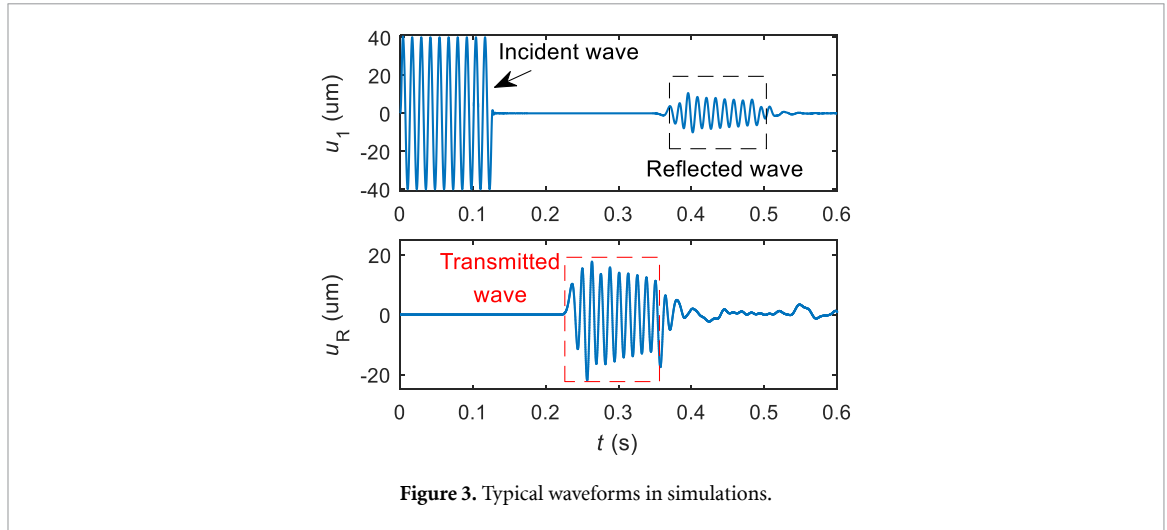


Figure 3. Typical waveforms in simulations.

Then, replacing F with $m_{\text{eff,L}}\ddot{u}_B$ in equation (7) gives the interaction equation:

$$m_{\text{eff,L}}\ddot{u}_B = -k_B u_B - k_{0I} \left. \frac{\partial(u_i + u_r)}{\partial x} \right|_{x=0} + k_{0II} \left. \frac{\partial u_t}{\partial x} \right|_{x=0}. \quad (8)$$

To solve this equation, let us specify

$$\begin{aligned} u_B &= U_B e^{i\omega t} \\ u_i(x, t) &= u_{ia} e^{i(\omega t - q_1 x)} \\ u_r(x, t) &= u_{ra} e^{i(\omega t + q_1 x)} \\ u_t(x, t) &= u_{ta} e^{i(\omega t - q_2 x)}. \end{aligned} \quad (9)$$

By substituting these variables into equation (8), one has,

$$(k_B - \omega^2 m_{\text{eff,L}}) U_B = ik_0 (q_1 u_{ia} - q_1 u_{ra} - q_2 u_{ta}). \quad (10)$$

Moreover, based on the continuity of displacement at the incident and transmission boundaries, one obtains boundary conditions:

$$\begin{aligned} u_i(x, t) + u_r(x, t) &= u_t(x, t) \Big|_{x=0} \\ u_t(x, t) \Big|_{x=0} &= u_B. \end{aligned} \quad (11)$$

Here we consider the case when $q_1 = q_2 = q$. Combing the two equations gives the transmission loss:

$$T_L = 20 \log_{10} \left| \frac{u_{ia}}{u_{ta}} \right| = 20 \log_{10} \left| 1 + \frac{k_B - \omega^2 m_{\text{eff,L}}}{i2k_0 \omega / c_0} \right| \quad (\text{dB}). \quad (12)$$

Moreover, by replacing $m_{\text{eff,L}}$ with m_B or m_t , we can study the influences of mass and boundary stiffness k_B on the wave insulation, which is termed as mass law. Equation (12) indicates that $T_L = 0$ dB for $k_B = \omega^2 m_{\text{eff,L}}$. This frequency is termed as the coincident frequency, f_{co} .

Furthermore, considering wave propagation in a 'medium' consisting of the periodic 3DoF cells in figure 1(b), the wave equation is

$$m_{\text{eff,L}} \frac{\partial^2 u}{\partial t^2} + k_B u = k_0 \frac{\partial^2 u}{\partial x^2}. \quad (13)$$

The solution of equation (13) denotes $u = u_a e^{i(\omega t \pm q_{\text{eff}} x)}$, where q_{eff} denotes the equivalent wave vector of such medium,

$$q_{\text{eff}} = \sqrt{(\omega^2 m_{\text{eff,L}} - k_B) / k_0}. \quad (14)$$

If the imaginary part $|\text{Im}(q_{\text{eff}})| > 0$, wave attenuates quickly, thus giving the corresponding frequency range referred to as bandgap.

2.4. Analytical method for nonlinear model

For the nonlinear model, we specify $g = y - u_B$, $s = z - y$ to simplify the equation (4) as

$$\begin{cases} m_B \ddot{u}_B = k_1 g + k_{1N} g^3 + F \\ m_1 (\ddot{u}_B + \ddot{g}) = -k_1 g - k_{1N} g^3 + k_2 s + k_{2N} s^3 \\ m_2 (\ddot{u}_B + \ddot{g} + \ddot{s}) = -k_2 s - k_{2N} s^3 \end{cases} \quad (15)$$

It is challenging to solve these nonlinear equations with boundary conditions. We propose a complete nonlinear method based on the first-order harmonic balance method.

2.4.1. Complete nonlinear method

First, we can directly solve the interaction equations by specifying the variables as below:

$$\begin{aligned} u_B &= A \sin \omega t + B \cos \omega t, \\ g &= G_1 \sin \omega t + G_2 \cos \omega t, \\ s &= S_1 \sin \omega t + S_2 \cos \omega t \\ F &= F_1 \sin \omega t + F_2 \cos \omega t \\ u_i(x, t) &= u_{ia} \sin(\omega t - q_1 x) \\ u_r(x, t) &= u_{ra1} \sin(\omega t + q_1 x) + u_{ra2} \cos(\omega t + q_1 x) \\ u_t(x, t) &= u_{ta1} \sin(\omega t - q_2 x) + u_{ta2} \cos(\omega t - q_2 x). \end{aligned} \quad (16)$$

High-order harmonics are not taken into consideration. By substituting equation (16) into equation (15), one obtains six equations with the first-order harmonic balance,

$$\begin{cases} -\omega^2 m_B A = k_1 G_1 + 0.75 k_{1N} (G_1^3 + G_1 G_2^2) + F_1 \\ -\omega^2 [(m_B + m_1 + m_2) A + (m_1 + m_2) G_1 + m_2 S_1] = F_1 \\ -\omega^2 m_2 (A + G_1 + S_1) = -k_2 S_1 - 0.75 k_{2N} (S_1^3 + S_1 S_2^2) \\ -\omega^2 m_B B = k_1 G_2 + 0.75 k_{1N} (G_2^3 + G_2 G_1^2) + F_2 \\ -\omega^2 [(m_B + m_1 + m_2) B + (m_1 + m_2) G_2 + m_2 S_2] = F_2 \\ -\omega^2 m_2 (B + G_2 + S_2) = -k_2 S_2 - 0.75 k_{2N} (S_2^3 + S_2 S_1^2) \end{cases} \quad (17)$$

Moreover, by substituting equation (16) into equation (6) and specifying $q_1 = q_2 = q$, one obtains:

$$\begin{cases} F_1 = -k_B A - 0.75 k_{BN} (A^3 + AB^2) + q k_0 (u_{ta2} + u_{ra2}) \\ F_2 = -k_B B - 0.75 k_{BN} (B^3 + BA^2) - q k_0 (u_{ta1} + u_{ra1} - u_{ia}) \end{cases} \quad (18)$$

Based on the boundary conditions described by equation (11), one has:

$$u_{ta1} = u_{ra1} + u_{ia} = A, \quad u_{ra2} = u_{ta2} = B. \quad (19)$$

Substituting equation (19) into equation (18) yields

$$\begin{cases} F_1 = -k_B A - 0.75 k_{BN} (A^3 + AB^2) + 2q k_0 B \\ F_2 = -k_B B - 0.75 k_{BN} (B^3 + BA^2) - 2q k_0 (A - u_{ia}) \end{cases} \quad (20)$$

At last, replacing F_1 and F_2 in equation (20) by equation (17), we can solve the six unknown variables A , B , G_1 , G_2 , S_1 , S_2 for any given incident wave amplitude u_{ia} .

Specifying vectors $\mathbf{u} = [A \ G_1 \ S_1]^T$, $\mathbf{v} = [B \ G_2 \ S_2]^T$, we can re-write the algebraic equations into matrices as:

$$\begin{cases} (\mathbf{K} - \omega^2 \mathbf{M}) \mathbf{u} - \mathbf{C} \mathbf{v} + \mathbf{N} (\mathbf{u}^2 + \mathbf{v}^2) \mathbf{u} = \mathbf{0} \\ (\mathbf{K} - \omega^2 \mathbf{M}) \mathbf{v} + \mathbf{C} \mathbf{u} + \mathbf{N} (\mathbf{u}^2 + \mathbf{v}^2) \mathbf{v} = \mathbf{u}_{in} \end{cases} \quad (21)$$

in which,

$$\mathbf{M} = \begin{bmatrix} m_B & 0 & 0 \\ m_B + m_1 + m_2 & m_1 + m_2 & m_2 \\ m_2 & m_2 & m_2 \end{bmatrix}, \mathbf{K} = \begin{bmatrix} k_B & -k_1 & 0 \\ k_B & 0 & 0 \\ 0 & 0 & k_2 \end{bmatrix}, \mathbf{C} = \frac{2\omega}{c} \begin{bmatrix} k_0 & 0 & 0 \\ k_0 & 0 & 0 \\ 0 & 0 & 0 \end{bmatrix},$$

$$\mathbf{N} = 0.75 \begin{bmatrix} k_{BN} & -k_{1N} & 0 \\ k_{BN} & 0 & 0 \\ 0 & 0 & k_{2N} \end{bmatrix}, \mathbf{u}_{in} = \frac{2\omega}{c} \begin{bmatrix} k_0 \\ k_0 \\ 0 \end{bmatrix} u_{ia}.$$

The equations can be analytically solved. We note that there is only one real number but several complex number solutions. Bifurcations occur when different branches of periodic solutions cross. Given the fact that these periodic solutions rely on stability analysis [46], we adopt the theory proposed by Fang *et al* in [47] to analyze the stability of a solution based on harmonic balance method. The Jacobian matrix \mathbf{J} for a periodic motion is

$$\mathbf{J} = \begin{bmatrix} -\mathbf{M}^{-1} & 0 \\ 0 & \mathbf{M}^{-1} \end{bmatrix} \begin{bmatrix} \mathbf{C} + \mathbf{N} \circ [[2\mathbf{u}\mathbf{v}]] & \mathbf{K} - \omega^2 \mathbf{M} + \mathbf{N} \circ [[\mathbf{u}^2 + 3\mathbf{v}^2]] \\ \mathbf{K} - \omega^2 \mathbf{M} + \mathbf{N} \circ [[3\mathbf{u}^2 + \mathbf{v}^2]] & -\mathbf{C} + \mathbf{N} \circ [[2\mathbf{u}\mathbf{v}]] \end{bmatrix}. \quad (22)$$

In which the notation $[[\mathbf{x}]]$ stands for the square matrix built upon the vector \mathbf{x} ; the expression $\mathbf{A} \circ \mathbf{B}$ denotes the element product of two matrices \mathbf{A} and \mathbf{B} . If the real part of an eigenvalue of \mathbf{J} is positive, the corresponding solution is unstable. Otherwise, the solution is stable. Note that a real number solution of equation (21) may be unstable, and a complex solution may be stable.

Furthermore, the transmission loss is:

$$T_L = 20 \log_{10} \left[u_{ia} / \sqrt{A^2 + B^2} \right]. \quad (23)$$

For linear cases, results from equations (23) and (12) are the same. The nonlinear effective mass is

$$m_{\text{eff}} = -(F_1 + iF_2) / \omega^2 (A + iB). \quad (24)$$

As confirmed, for linear systems, solutions from equations (23) and (12) are equal.

2.4.2. Equivalent linear method

In addition, because the stiffness coefficients between the oscillators m_B, m_1, m_2 are tuned by nonlinear interactions, we can build an equivalent linear model of the nonlinear model, i.e. the equivalent linearized approach. For this, supposing the equivalent linear stiffness are $k_{1\text{eq}} = \gamma_1 k_1, k_{2\text{eq}} = \gamma_2 k_2, k_{B\text{eq}} = \gamma_3 k_B$, where γ_i is an approximate factor. By substituting k_i with $k_{i\text{eq}}$ in equation (7), one gets the effective mass of the equivalent linearized system as:

$$m_{\text{eff,L}}^{(\text{eq})} = m_B + \frac{k_{2\text{eq}} \omega_{1\text{eq}}^2 + k_{1\text{eq}} (\omega_{2\text{eq}}^2 - \omega^2)}{(\omega_{1\text{eq}}^2 - \omega^2)(\omega_{2\text{eq}}^2 - \omega^2) - \omega^2 k_{2\text{eq}} / m_1}. \quad (25)$$

Then we can obtain the wave insulation of the linearized system with equation (12).

3. Wave insulation of linear model

Before investigating nonlinear models, we recall the properties of wave insulation of linear structural or metamaterials, as shown in figure 4. Two other cases, $m_{\text{eff,L}} = m_B$ and $m_{\text{eff,L}} = m_t$, are also depicted in figure 4. Numerical results agree with the analytical curves, which confirms the validity of analytical method. There are three coincident frequencies, $f_{\text{co1}} < f_{\text{co2}} < f_{\text{co3}}$. Owing to the boundary stiffness $k_B \neq 0$, waves in $0 \sim f_{\text{co1}}$ are greatly insulated because $|\text{Im}(q_{\text{eff}})| > 0$ in $0 \sim f_{\text{co1}}$, as indicated in figure 4(b). This is the stiffness-dominant band. The range $f > f_{\text{co1}}$ is termed as mass-dominant band, in which T_L increases by 6 dB when the mass is doubled. Two insulation peaks appear near the locally resonant frequencies, f_{r1} and f_{r2} , and the peaks exceed the mass law limit corresponding to $m_{\text{eff,L}} = m_t$. Figure 4(c) and equation (12) indicate that the high transmission loss appears in the band for $|k_B - \omega^2 m_{\text{eff,L}}| \gg 2k_0 \omega / c_0$, which means $m_{\text{eff,L}} \rightarrow \pm\infty$. Therefore, the insulation peaks near f_{r1} and f_{r2} are generated by the mass amplification arising from the local resonances. However, as stated in introduction, in linear model, every narrow insulation peak is accompanied by a broad insulation valley near the coincident frequency. T_L in valleys is much smaller than curves for $m_{\text{eff,L}} = m_B$ and $m_{\text{eff,L}} = m_t$.

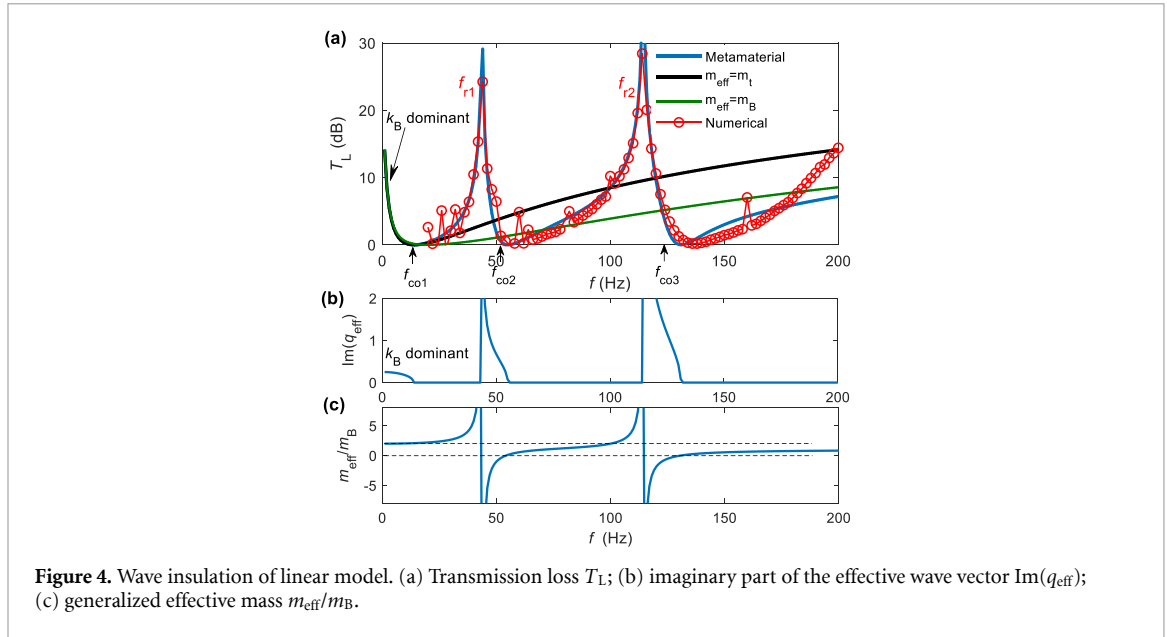


Figure 4. Wave insulation of linear model. (a) Transmission loss T_L ; (b) imaginary part of the effective wave vector $\text{Im}(q_{\text{eff}})$; (c) generalized effective mass m_{eff}/m_B .

Table 1. Four nonlinear cases.

Cases	Parameters
Case A: remote nonlinear local resonator	$k_{BN} = 0, k_{1N} = 0, k_{2N} \neq 0$
Case B: close nonlinear local resonator	$k_{BN} = 0, k_{1N} \neq 0, k_{2N} = 0$
Case C: both close and remote nonlinear local resonators	$k_{BN} = 0, k_{1N} \neq 0, k_{2N} \neq 0$
Case D: completely nonlinear model	$k_{BN} \neq 0, k_{1N} \neq 0, k_{2N} \neq 0$

4. Wave insulation of nonlinear models

Four types of nonlinear interaction are considered, where nonlinearity is imposed at different positions. As listed in table 1, they are distinguished by the nonlinear boundary, remote nonlinear local resonator (nonlinearity at m_2), close nonlinear local resonator (nonlinearity at m_1), and completely nonlinear model (nonlinearity acts at all positions).

4.1. Case A: remote nonlinear local resonator

The bifurcation analyses of model A with typical variables, $k_{2N} = 3 \times 10^{10}$ and $k_{2N} = 1 \times 10^{13} \text{ N m}^{-3}$, are shown in figure 5, alongside the wave insulation properties shown in figure 6. We combine figures 5 and 6 to clarify the phenomena and the underlying physical mechanisms. Similar figures are presented for other cases.

As shown in figure 5, there is a saddle node bifurcation point, marked by f_B , in the wave insulation curve T_L and the generalized effective mass $|m_{\text{eff}}/m_t|$ curve. For $f < f_B$, there are two analytical branches: the branch with real number solution is stable (red circles); the other complex solution is unstable (black circles). Therefore, the numerical result will follow the first stable branch for $f < f_B$. For $f > f_B$, there are three branches, 1, 2, 3. The real number solution on branch 1 becomes unstable, while the complex branch 2 is stable. Therefore, there may be a jump from branch 1 to branch 2 at $f = f_B$.

For clarity, besides the numerical results, only the real number analytical solutions are present in figure 6. Analytical curves agree well with numerical results. The numerical responses mainly follow with the real number solution. The influences of the nonlinear coefficient k_{2N} on the transmission loss are shown in figure 6(b). Changing k_{2N} first alters the frequency of the resonator m_2 , whose frequency is lower than m_1 . When increasing k_{2N} from 1×10^{10} to $1 \times 10^{13} \text{ N m}^{-3}$, the first insulation peak always exists but its frequency increases gradually from 44 to 66 Hz. The second insulation peak first shifts a little to higher frequencies, but a moderate nonlinearity ($k_{2N} = 3 \times 10^{10}$) changes the trends. For $k_{2N} = 3 \times 10^{10}$, the insulation peak near 180 Hz, as predicted by analytical solutions, is not generated in numerical T_L because this peak corresponding to the unstable solution in figure 5(a). Instead, as predicted by the bifurcation jump in figure 5(a), the numerical T_L features a jump near 140 Hz. As shown in figure 6(a), further increasing $k_{2N} > 3 \times 10^{10}$ will diminish the second insulation peak until it completely disappears, so that only a low frequency insulation peak is left. The equivalent linearized theory shows that this peak is formed when $k_2 \rightarrow +\infty$, indicating that it happens because enhancing the hardening nonlinearity merges the two

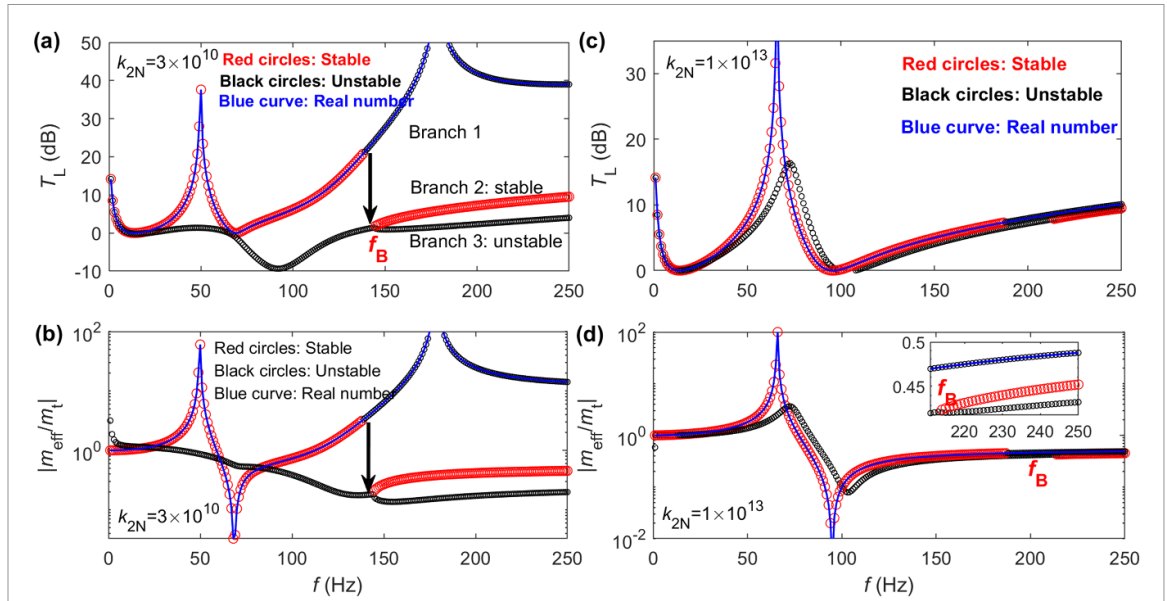


Figure 5. Bifurcation of analytical solutions in model A. (a), (c) Wave insulation T_L . (b), (d) Generalized effective mass $|m_{eff}/m_t|$. (a), (b) $k_{2N} = 3 \times 10^{10} \text{ N m}^{-3}$. (c), (d) $k_{2N} = 1 \times 10^{13} \text{ N m}^{-3}$. In these panels, red circles and black circles represent stable and unstable solutions, respectively. The circles connected by blue curves represent the real number solutions.

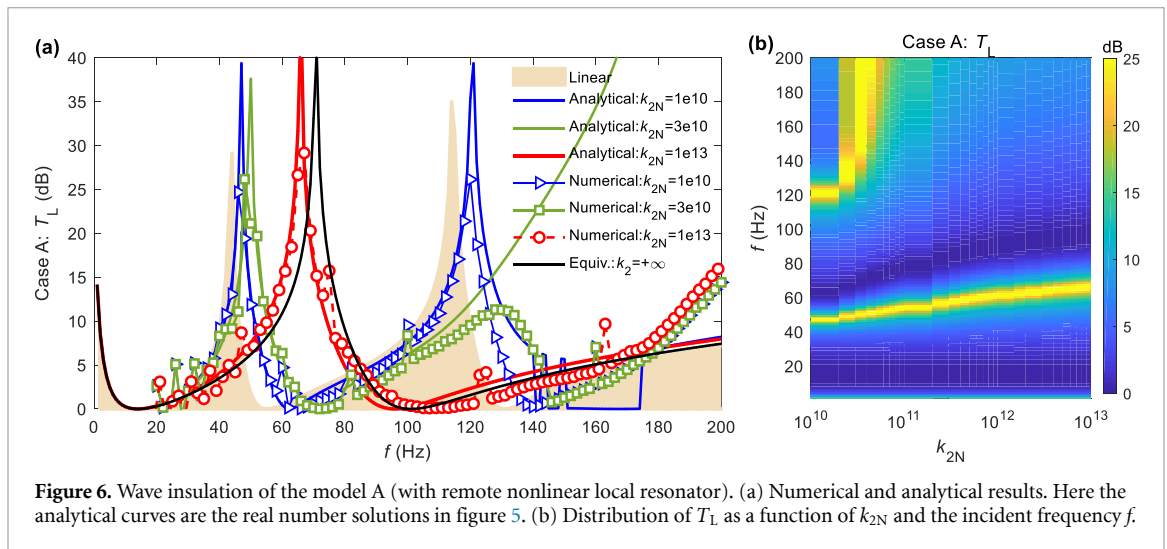


Figure 6. Wave insulation of the model A (with remote nonlinear local resonator). (a) Numerical and analytical results. Here the analytical curves are the real number solutions in figure 5. (b) Distribution of T_L as a function of k_{2N} and the incident frequency f .

resonators into one. The bandwidth of this peak is broadened: the band for $T_L > 10 \text{ dB}$ increases from 40–46 to 55–76 Hz.

Moreover, the frequency ranges, relating to the shifting and disappearing of the wave insulation peaks in figures 5(a), (c) and 6, are in accordance with the varying trend of the super mass $|m_{eff}/m_t| > 1$ in figures 5(b) and (d). Except for the insulation in the stiffness dominant band for $f < f_{c01} = 20 \text{ Hz}$ here, we can always obtain $T_L \propto |m_{eff}/m_t|$ along the stable branches. Therefore, the amplified super mass due to local resonances remains the essential mechanism for the high sound insulation of nonlinear model A.

However, in Case A, the nonlinear interaction between m_1 and m_2 cannot offer broader-band wave insulation than the equivalent linearized model (see the black curve in figure 6(a)). This means the nonlinear model A cannot provide better insulation capability than a proper linear system with same mass. Moreover, the spectra of the transmitted waves at the insulation peaks in figure 7 show that many high-order harmonics are generated by strong nonlinearity.

4.2. Case B: close nonlinear local resonator

In Case B, nonlinearity only acts between m_1 and m_B , $k_{1N} > 0$, $k_{2N} = 0$. We combine the bifurcation analysis in figure 8 and numerical results in figure 9 to show the physical phenomena. As shown in figure 9(b), the first insulation peak nearly persists when increasing k_{1N} . The second insulation peak shifts upwards, but will not disappear as what happens in Case A. As shown in figure 8, the model gives two or three analytical

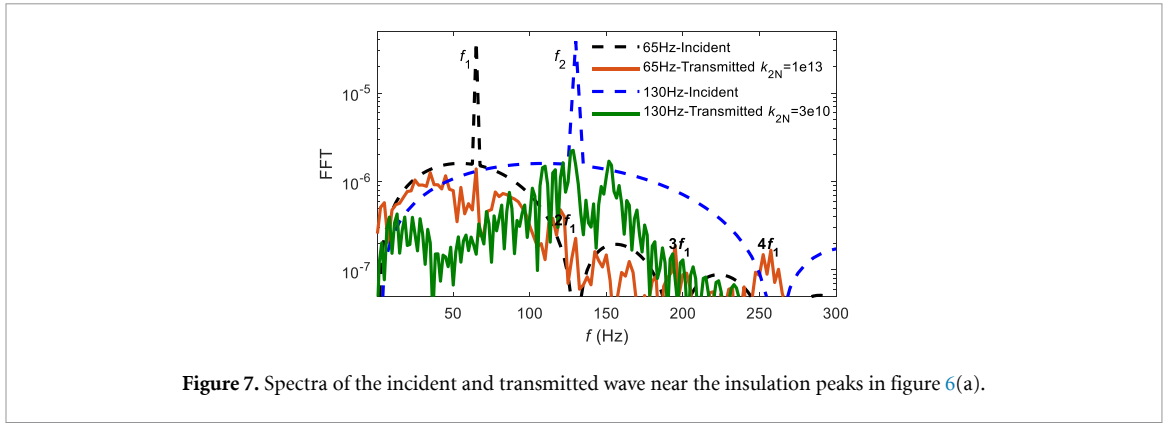


Figure 7. Spectra of the incident and transmitted wave near the insulation peaks in figure 6(a).

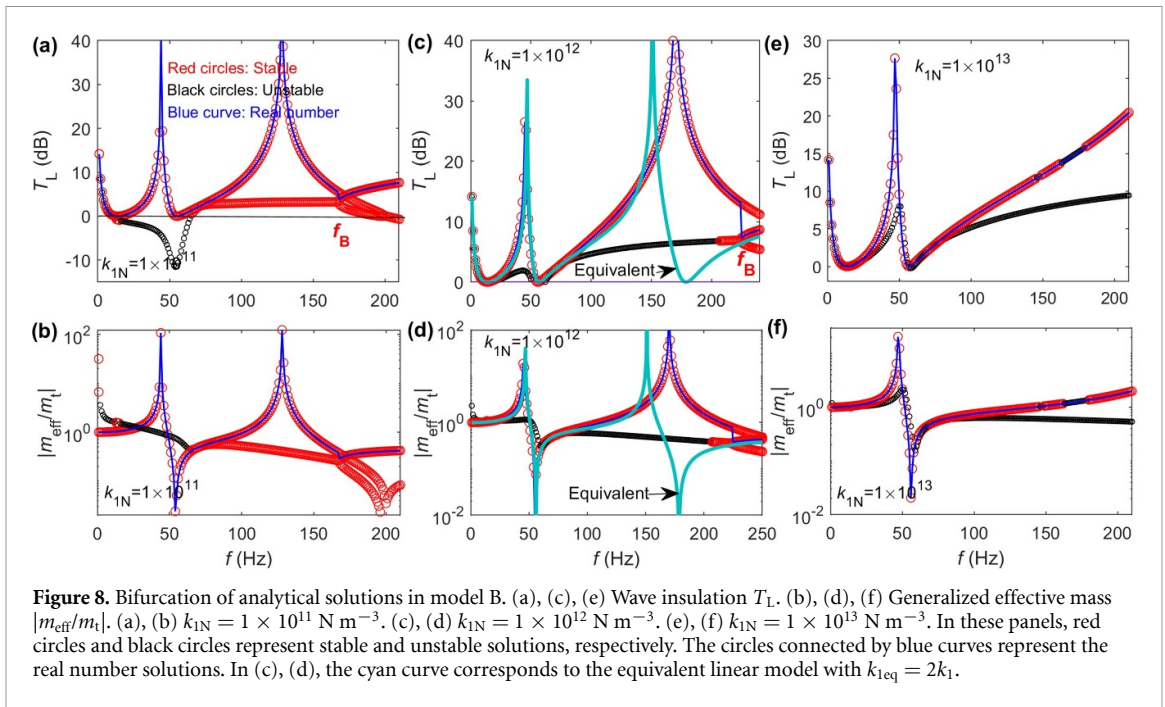


Figure 8. Bifurcation of analytical solutions in model B. (a), (c), (e) Wave insulation T_L . (b), (d), (f) Generalized effective mass $|m_{\text{eff}}/m_t|$. (a), (b) $k_{1N} = 1 \times 10^{11} \text{ N m}^{-3}$. (c), (d) $k_{1N} = 1 \times 10^{12} \text{ N m}^{-3}$. (e), (f) $k_{1N} = 1 \times 10^{13} \text{ N m}^{-3}$. In these panels, red circles and black circles represent stable and unstable solutions, respectively. The circles connected by blue curves represent the real number solutions. In (c), (d), the cyan curve corresponds to the equivalent linear model with $k_{1\text{eq}} = 2k_1$.

solutions for each given frequency, and the bifurcation depends on k_{1N} . For $k_{1N} = 1 \times 10^{11}$, all three branches after the bifurcation frequency f_B are stable, but two of them lead to negative insulation T_L that will not occur in practice. Therefore, as demonstrated by the numerical result in figure 9(a), the practical curve follows the highest T_L with the real number solution. For $k_{1N} = 1 \times 10^{12}$, the real number solution in $f < f_B$ is stable, and the middle branch in $f > f_B$ is stable, indicating a jump at $f = f_B$. For $k_{1N} = 1 \times 10^{13}$, the second peak is shifted to high frequency; the curve with higher T_L is stable in most part of the frequency range, with T_L increasing with the frequency in 60–220 Hz. This is also demonstrated in figure 9(a). Still on this curve, stable and unstable solutions appear alternately near 170 Hz, so the numerical results fluctuate. Therefore, numerical results still agree well with analytical curves with stable and real number solutions.

More importantly, the solutions for both the first and the second insulation peaks remain stable in model B (the second peak for model A is unstable). Therefore, model B can provide two insulation peaks. Interestingly, both the bandwidth and transmission loss of the second peak are greatly increased along with the increasing k_{1N} . Meanwhile, the coincidence effect behind the second peak also disappears even with weak nonlinearity, $k_{1N} = 1 \times 10^{11}$. This happens because of the bifurcation in figures 8(a) and (b). As a result, T_L in the insulation valley increases by more than 10 dB under strong nonlinearity. Furthermore, we check whether an equivalent linearized model can realize this effect. As shown in figures 8(c), (d) and 9(a), we tune $k_{1\text{eq}} = 2k_1$ to make the equivalent linear model approximately gets the same initial frequency for $T_L > 10$ dB near the second peak of the nonlinear model $k_{1N} = 1 \times 10^{12}$. The band for $T_L > 10$ dB of the linear model is 125–168 Hz, while it is 120–200 Hz for the nonlinear model with $k_{1N} = 1 \times 10^{12}$, 1.86 times broader. Therefore, the nonlinear model B can eliminate a coincident effect and present broader wave insulation with the same mass.

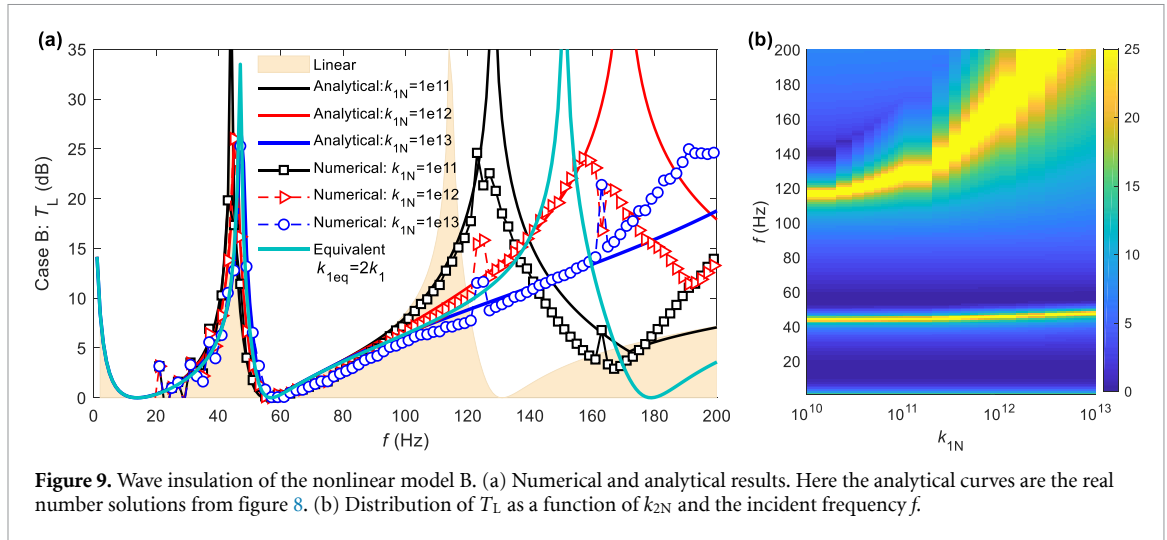


Figure 9. Wave insulation of the nonlinear model B. (a) Numerical and analytical results. Here the analytical curves are the real number solutions from figure 8. (b) Distribution of T_L as a function of k_{2N} and the incident frequency f .

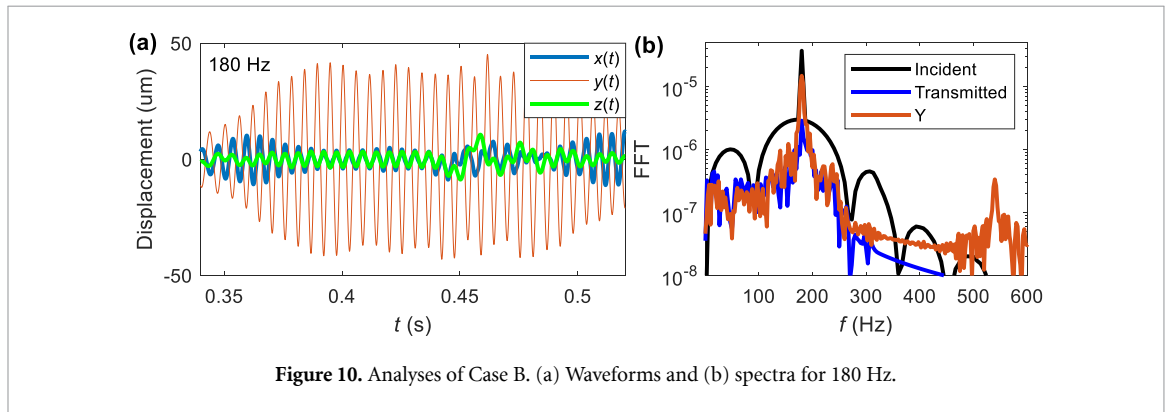


Figure 10. Analyses of Case B. (a) Waveforms and (b) spectra for 180 Hz.

Furthermore, we analyze the responses at 180 Hz and the effective mass for $k_{1N} = 1 \times 10^{12}$, as shown in figure 10. The waveforms and spectra suggest that the incident and transmitted waves have the same main frequency, and high-order harmonics are not remarkable. Therefore, the frequency is nearly preserved. The high-order harmonics in the transmitted is suppressed because their frequencies locate in the bandgap of phononic I and II, i.e. $3f > f_{\text{gap}}$. As illustrated in figure 8, the peaks of $|m_{\text{eff}}/m_i|$ are consistent with the insulation peaks, and their varying trends are also same when enhancing nonlinearity. Therefore, the broader and greater wave insulation of nonlinear model B stems from the broader band of super mass induced by strongly nonlinear local resonances. The mechanism is consistent with model A.

4.3. Case C: both close and remote nonlinear local resonators

In this section, we consider the nonlinear interaction appears at both the remote and close local resonators, and $k_{1N} = k_{2N} > 0$ is specified here. As shown in figure 11, this model has seven analytical branches, which result in many bifurcations. Fortunately, only the branch featuring the first insulation peak is stable in $f < f_B$; and only one branch stemming from the saddle node bifurcation point f_B is stable, i.e. jumping happens here. As shown in figure 12, analytical curves agree with numerical solutions very well, including the jumping at $f_B = 162$ Hz for $k_{1N} = k_{2N} = 5 \times 10^{10}$.

In whole (figure 12(b)), while increasing the nonlinear coefficient from 1×10^{10} to 1×10^{13} , the first insulation peak gradually shifts from 47 Hz to 120 Hz; the second insulation peak shifts upwards first, but diminishes when $k_{1N} = k_{2N} > 1 \times 10^{11}$. The second peak diminishes because the periodic solution becomes unstable at this peak, as illustrated in figure 11(a), like in Case A. Properties of cases A and C indicate that the second peak will be suppressed under moderate nonlinearity if there is nonlinearity in resonator m_2 .

Under strong nonlinearity (described by $k_{1N} = k_{2N} = 1 \times 10^{13}$ or 1×10^{14}), though there is only one insulation peak, the nonlinear model offers very broad and extremely high wave insulation that breaks through the mass law for $m_{\text{eff}} = m_1$. Taking $k_{1N} = k_{2N} = 1 \times 10^{13}$ as example, the equivalent linearized model has $T_L > 10$ dB in 80–126 Hz, but it is 72–200 Hz for the nonlinear model. The generalized bandwidth $(f_{\text{end}}/f_{\text{start}} - 1)$ is broadened by three times by strong nonlinearity and the insulation valley is also eliminated. Solutions for $k_{1N} = k_{2N} = 1 \times 10^{14}$ in figure 12(c) validate the enhanced wave insulation.

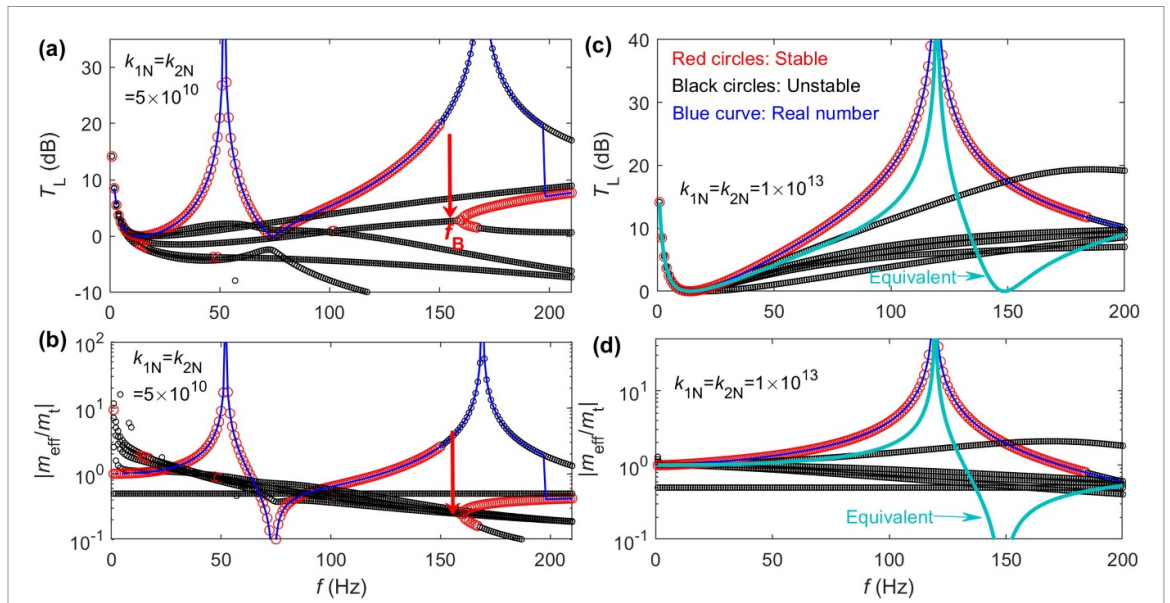


Figure 11. Bifurcation of analytical solutions in model C. (a) and (c) Wave insulation T_L . (b) and (d) Generalized effective mass $|m_{\text{eff}}/m_t|$. (a) and (b) $k_{1N} = k_{2N} = 5 \times 10^{10} \text{ N m}^{-3}$. (c) and (d) $k_{1N} = k_{2N} = 1 \times 10^{13} \text{ N m}^{-3}$. Red circles and black circles represent stable and unstable solutions, respectively. In (c), (d), the cyan curve corresponding to the results of the equivalent linear model.

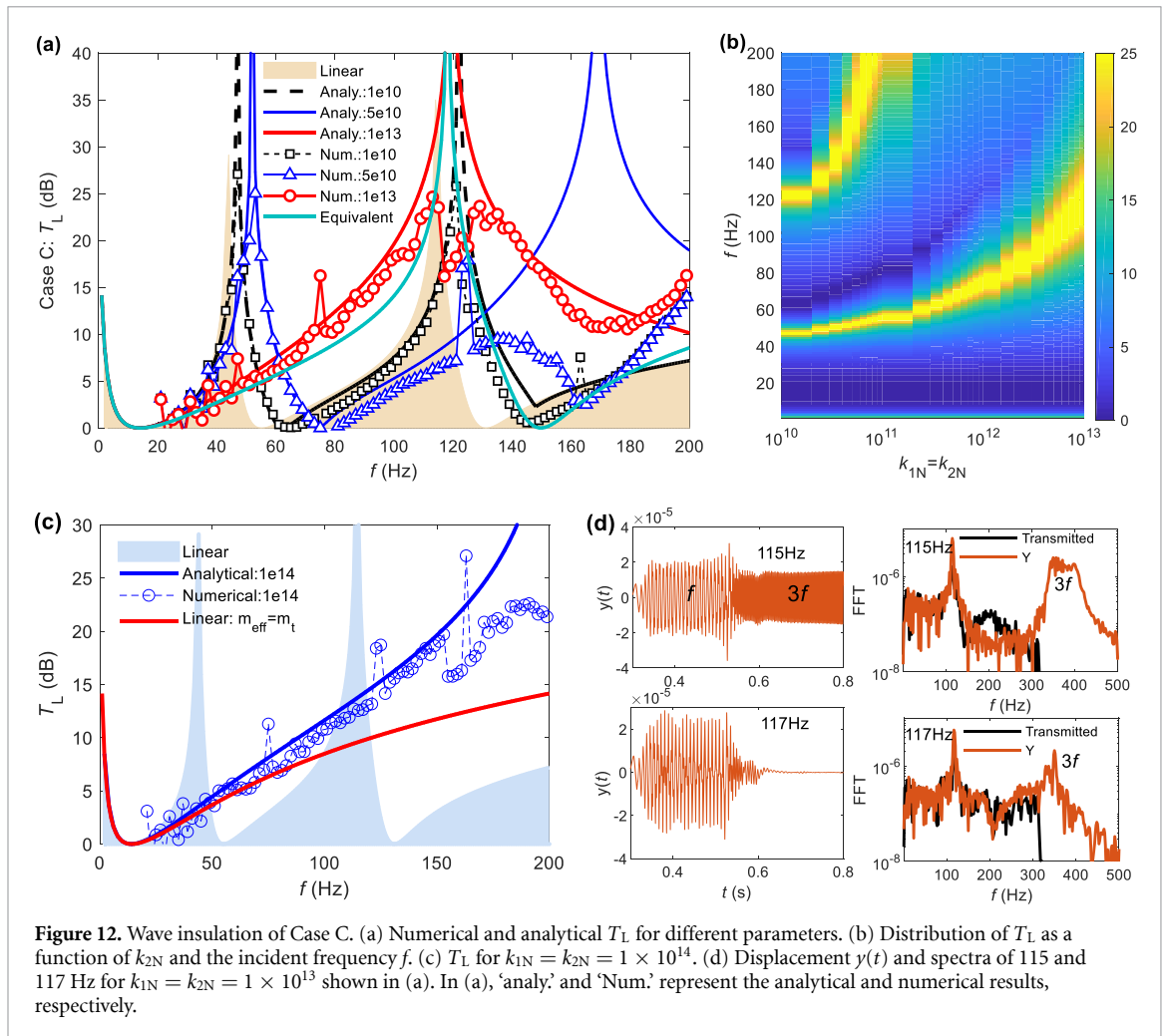


Figure 12. Wave insulation of Case C. (a) Numerical and analytical T_L for different parameters. (b) Distribution of T_L as a function of k_{2N} and the incident frequency f . (c) T_L for $k_{1N} = k_{2N} = 1 \times 10^{14}$. (d) Displacement $y(t)$ and spectra of 115 and 117 Hz for $k_{1N} = k_{2N} = 1 \times 10^{13}$ shown in (a). In (a), ‘analy.’ and ‘Num.’ represent the analytical and numerical results, respectively.

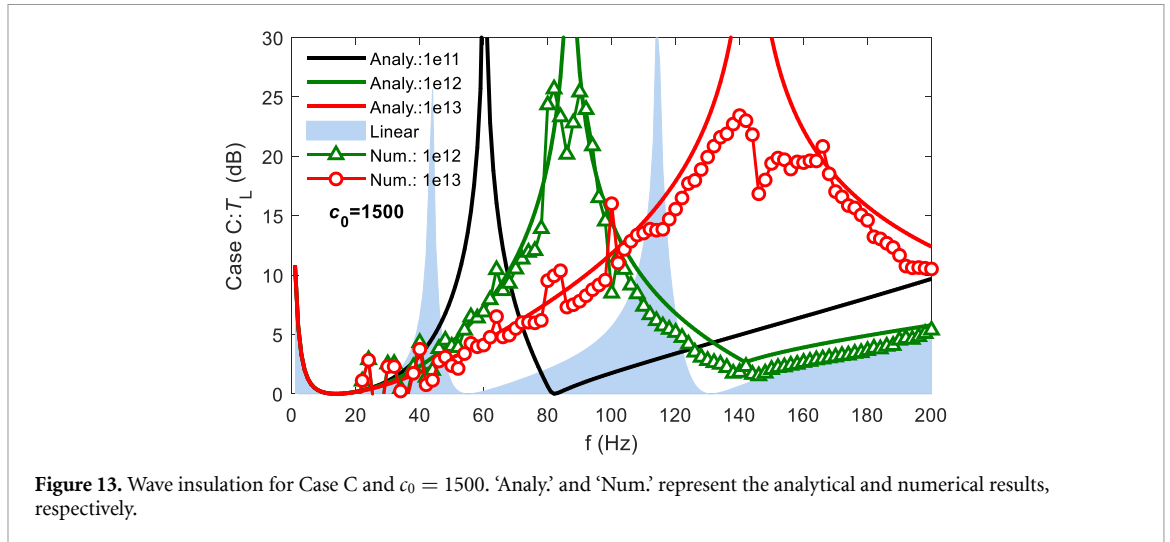


Figure 13. Wave insulation for Case C and $c_0 = 1500$. ‘Analy.’ and ‘Num.’ represent the analytical and numerical results, respectively.

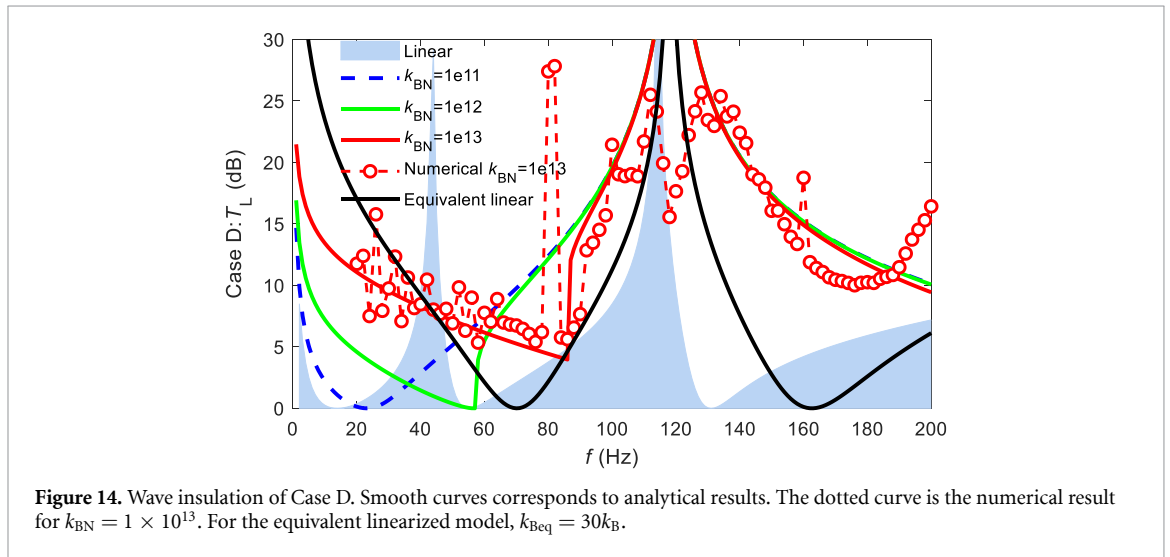


Figure 14. Wave insulation of Case D. Smooth curves corresponds to analytical results. The dotted curve is the numerical result for $k_{BN} = 1 \times 10^{13}$. For the equivalent linearized model, $k_{Beq} = 30k_B$.

In figure 12(a), numerical curve for $k_{1N} = k_{2N} = 1 \times 10^{13}$ jumps near 116 Hz. As shown in figure 12(d), for $f = 115$ Hz before the jump, the nonlinear model generates remarkable third-order responses. When the fundamental wave transmits into phononic crystal II, the third harmonic is localized inside the nonlinear resonators because $3f$ locates in the bandgap of the crystals. Behind the jump (117 Hz), the third harmonic in the oscillators is not as large as the one at 115 Hz. The main difference between the two transmitted waves lies in the responses in 200–300 Hz.

Furthermore, we increase the wave speed c_0 to 1500 by increasing k_0 to study the influences of wave speed. As shown in figure 13, a broadband wave insulation of strongly nonlinear model is achieved again. These analyses confirm the generality of the enhanced insulation capability of the strongly nonlinear model which embed proper nonlinear interactions. Moreover, a jumping of T_L appears at the insulation peak again.

4.4. Case D: completely nonlinear model

At last, we study the model D with nonlinearity in two local resonator and the nonlinear boundary. Based on the results above, we specify $k_{1N} = k_{2N} = 1 \times 10^{13}$ and change k_{BN} in case D. Bifurcation analysis is not repeated here. As illustrated in figure 14, the influences of boundary nonlinearity mainly lie in the stiffness-dominant region and it has little effect on the insulation peak near 120 Hz. Increasing k_{BN} can greatly expand the stiffness dominant range. In cases B and C, only the coincident frequencies behind the resonant insulation peaks are eliminated by nonlinearity. Here, the coincident insulation valley between the stiffness and mass dominant bands are eliminated when k_{BN} is large. As predicted by the analytical method, T_L curve undergoes a drastic change at the junction between the two bands. The numerical results demonstrate these properties. However, compared with the equivalent linearized system by changing k_B , T_L induced by nonlinear model is smaller than the one in the linear model for $f \rightarrow 0$.

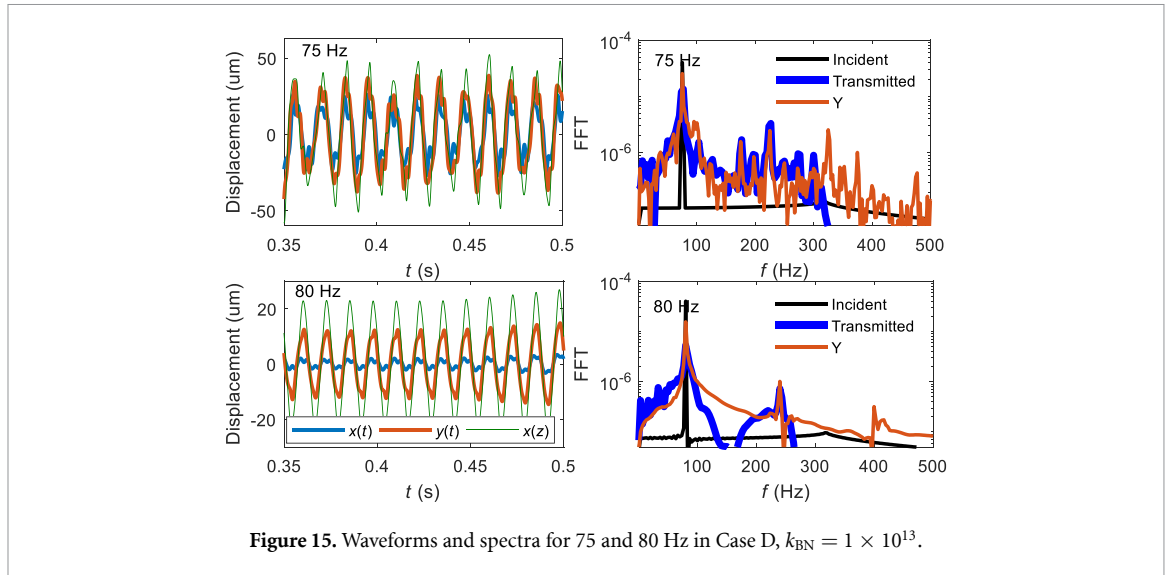


Figure 15. Waveforms and spectra for 75 and 80 Hz in Case D, $k_{BN} = 1 \times 10^{13}$.

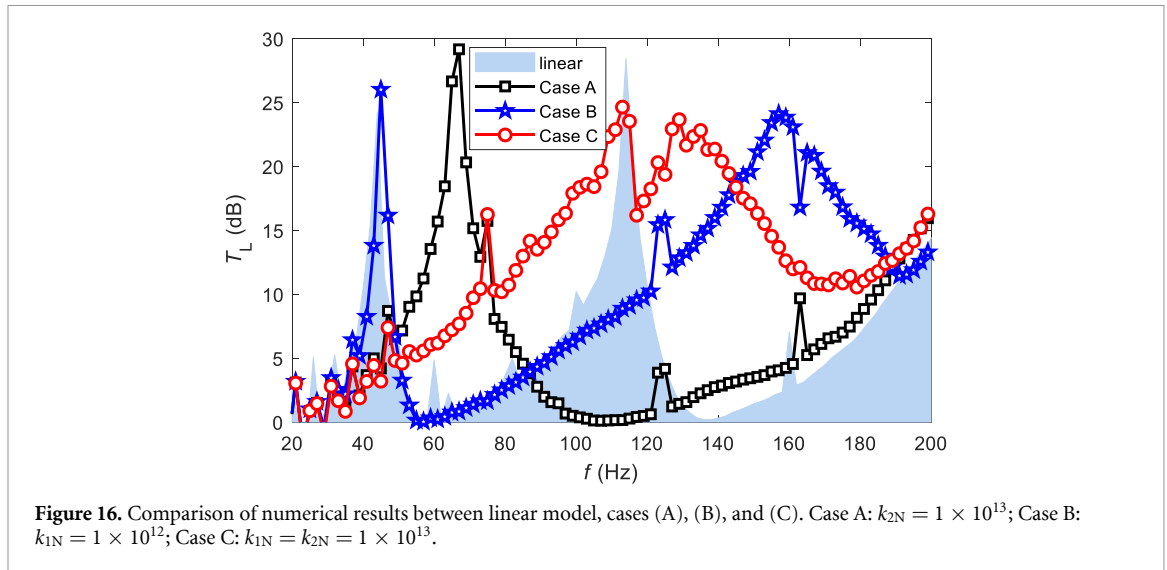


Figure 16. Comparison of numerical results between linear model, cases (A), (B), and (C). Case A: $k_{2N} = 1 \times 10^{13}$; Case B: $k_{1N} = 1 \times 10^{12}$; Case C: $k_{1N} = k_{2N} = 1 \times 10^{13}$.

Moreover, numerical curve T_L in figure 14 jumps from 6 dB to 27 dB in 80–82 Hz. We analyze the waveforms and spectra for before (75 Hz) and after (80 Hz) the jump, as shown in figure 15. At 75 Hz, there are high-order or even chaotic responses but the three oscillators, m_B , m_1 and m_2 , vibrate almost synchronously and their amplitudes are approximately equal, which means the local resonance in m_1 and m_2 is not formed. At 80 Hz, the motions are still synchronous but energy is localized in m_1 and m_2 . Therefore, the great insulation is generated by nonlinear local resonance.

4.5. Comparison of different nonlinear cases

Herein we briefly summarize the influences of different nonlinear interactions on the acoustic wave insulation. The optimal results for cases A, B and C are illustrated in figure 16:

- (i) When the nonlinear interaction only appears between m_1 and m_2 (case A), the wave insulation is not drastically improved with respect to the linear model.
- (ii) When strongly nonlinear interaction only appears between m_B and m_1 (case B), the low-frequency insulation peak remains; the coincident insulation valley after the second insulation peak is eliminated; the bandwidth for high insulation is expanded by two times.
- (iii) When there are strongly nonlinear interactions in both pairs m_B – m_1 and m_1 – m_2 (case C), the bandwidth for high insulation can be broadened by about three times.
- (iv) When strong boundary nonlinearity is introduced (case D), the coincident insulation valley between the stiffness and mass dominant bands are eliminated, but the transmission loss for $f \rightarrow 0$ becomes smaller than the one offered by equivalent linear model.

- (v) When nonlinearity exists at the boundary and two resonators, low-frequency and broadband wave insulation is achievable.

5. Conclusions

This paper reveals a possibility of breaking the mass law of wave insulation through exploring system nonlinearity, while broadening the frequency bandwidth for effective sound insulation. As illustration, a basic and typical 1D model, consisting of two local resonators and elastic boundaries, is established to simulate the acoustic/elastic wave insulation. Three nonlinear sources, placed in the boundary and two resonators, are respectively considered. Analytical methods for both linear and nonlinear model are proposed, and their accuracy is validated by numerical integration method. Bifurcation and stability of periodic solutions are performed. It is shown that the wave insulation efficacy closely depends on the location of nonlinearity. Influences of four typical types of nonlinear interactions are investigated with the underlying mechanisms explained.

Nonlinear interaction changes the wave insulation properties in different ways. By introducing proper strongly nonlinear interactions, especially strong nonlinearity between the primary mass and the first resonator attached on it, the bandwidth for superior wave insulation can be expanded by 2–3 times relative to the optimal linear model with the same mass (the equivalent linearized model). Meanwhile, the insulation valley arising from the coincident effects can also be eliminated. Moreover, the mechanism underpinning the observed broadened bandwidth for large wave insulation is elucidated by combining the bifurcations, stability, effective mass and equivalent linearized model. We establish that the observed broader and superior wave insulation offered by the strongly nonlinear model stems from the broader band of super mass induced by strongly nonlinear local resonances.

This study provides theoretical foundation for acoustic/elastic wave insulation in complex nonlinear structures, which can be extended to the metamaterial. It sheds lights on the underlying physics while offering a new way to design high performance light-weight structures for acoustic wave insulation.

Data availability statement

The data that support the findings of this study are available upon reasonable request from the authors.

Acknowledgments

This paper is funded by the National Natural Science Foundation of China (Projects No. 52322505, 52241103 and 12002371), and Natural Science Fund for Distinguished Young Scholars of Hunan Province (Project No. 2023JJ10055).

ORCID iDs

Xin Fang  <https://orcid.org/0000-0002-2655-3805>

Li Cheng  <https://orcid.org/0000-0001-6110-8099>

References

- [1] Sellappan P and Alvi F S 2022 Three-dimensional flow field and acoustics of supersonic rectangular jets *Exp. Fluids* **63** 20
- [2] Wang Z, Zang J and Zhang Y 2022 Method for controlling vibration and harvesting energy by spacecraft: theory and experiment *AIAA J.* **60** 6097–115
- [3] Cremer L and Heckl M 1988 *Structure-Borne Sound* (Springer)
- [4] Wang J 2022 *Active Vibration & Noise Control: Design Towards Performance Limit* (Springer)
- [5] Ding H and Chen L 2020 Designs, analysis, and applications of nonlinear energy sinks *Nonlinear Dyn.* **100** 3061–107
- [6] Vakakis A F, Gendelman O V, Bergman L A, Mojahed A and Gzal M 2022 Nonlinear targeted energy transfer: state of the art and new perspectives *Nonlinear Dyn.* **108** 711–41
- [7] Bellet R, Cochelin B, Herzog P and Mattei P O 2010 Experimental study of targeted energy transfer from an acoustic system to a nonlinear membrane absorber *J. Sound Vib.* **329** 2768–91
- [8] Mariani R, Bellizzi S, Cochelin B, Herzog P and Mattei P O 2011 Toward an adjustable nonlinear low frequency acoustic absorber *J. Sound Vib.* **330** 5245–58
- [9] Shao J and Cochelin B 2014 Theoretical and numerical study of targeted energy transfer inside an acoustic cavity by a non-linear membrane absorber *Int. J. Non-Linear Mech.* **64** 85–92
- [10] Wu X, Shao J and Cochelin B 2016 Study of targeted energy transfer inside three-dimensional acoustic cavity by two nonlinear membrane absorbers and an acoustic mode *J. Vib. Acoust.* **138** 031017
- [11] Bryk P Y, Bellizzi S and Côte R 2018 Experimental study of a hybrid electro-acoustic nonlinear membrane absorber *J. Sound Vib.* **424** 224–37
- [12] Shao J, Zhao H, Yang J, Luo Q and Wu X 2023 Research on suppressing radiation noise of plate inside acoustic cavity based on targeted energy transfer of nonlinear energy sink *J. Braz. Soc. Mech. Sci. Eng.* **45** 220

- [13] Liu Z, Zhang X, Mao Y, Zhu Y Y, Yang Z, Chan C T and Sheng P 2000 Locally resonant sonic materials *Science* **289** 1734–6
- [14] Lu Q, Li X, Zhang X, Lu M and Chen Y 2022 Perspective: acoustic metamaterials in future engineering *Engineering* **17** 22–30
- [15] Dong H, Zhao S, Wang Y, Cheng L and Zhang C 2020 Robust 2d/3d multi-polar acoustic metamaterials with broadband double negativity *J. Mech. Phys. Solids* **137** 103889
- [16] Gao P, Climent A, Sánchez-Dehesa J and Wu L 2019 Single-phase metamaterial plates for broadband vibration suppression at low frequencies *J. Sound Vib.* **444** 108–26
- [17] Xiao Y, Wen J, Wang G and Wen X 2013 Theoretical and experimental study of locally resonant and bragg band gaps in flexural beams carrying periodic arrays of beam-like resonators *J. Vib. Acoust.* **135** 41006
- [18] Zhou G, Wu J H, Lu K, Tian X, Huang W and Zhu K 2020 Broadband low-frequency membrane-type acoustic metamaterials with multi-state anti-resonances *Appl. Acoust.* **159** 107078
- [19] Zhang H, Chen S, Liu Z, Song Y and Xiao Y 2020 Light-weight large-scale tunable metamaterial panel for low-frequency sound insulation *Appl. Phys. Express* **13** 067003
- [20] Wang X, Chen Y, Zhou G, Chen T and Ma F 2019 Synergetic coupling large-scale plate-type acoustic metamaterial panel for broadband sound insulation *J. Sound Vib.* **459** 114867
- [21] Van Belle L, Claeys C, Deckers E and Desmet W 2019 The impact of damping on the sound transmission loss of locally resonant metamaterial plates *J. Sound Vib.* **461** 114909
- [22] Liao Y, Chen Y, Huang G and Zhou X 2018 Broadband low-frequency sound isolation by lightweight adaptive metamaterials *J. Appl. Phys.* **123** 91705
- [23] Song Y, Feng L, Wen J, Yu D and Wen X 2015 Reduction of the sound transmission of a periodic sandwich plate using the stop band concept *Compos. Struct.* **128** 428–36
- [24] Zhang H, Xiao Y, Wen J, Yu D and Wen X 2016 Ultra-thin smart acoustic metasurface for low-frequency sound insulation *Appl. Phys. Lett.* **108** 141902
- [25] Fang X, Wen J, Yin J, Yu D and Xiao Y 2016 Broadband and tunable one-dimensional strongly nonlinear acoustic metamaterials: theoretical study *Phys. Rev. E* **94** 52206
- [26] Fang X, Wen J, Yin J and Yu D 2016 Wave propagation in nonlinear metamaterial multi-atomic chains based on homotopy method *AIP Adv.* **6** 121706
- [27] Patil G U and Matlack K H 2022 Review of exploiting nonlinearity in phononic materials to enable nonlinear wave responses *Acta Mech.* **233** 1–46
- [28] Bonnefois J J, Guida G, Priou A, Nevière M and Popov E 2006 Simulation of two-dimensional Kerr photonic crystals via fast Fourier factorization *J. Opt. Soc. Am. A* **23** 842–7
- [29] Jiao W and Gonella S 2019 Doubly nonlinear waveguides with self-switching functionality selection capabilities *Phys. Rev. E* **99** 42206
- [30] Zhou J, Dou L, Wang K, Xu D and Ouyang H 2019 A nonlinear resonator with inertial amplification for very low-frequency flexural wave attenuations in beams *Nonlinear Dyn.* **96** 647–65
- [31] Fang X, Wen J, Yu D, Huang G and Yin J 2018 Wave propagation in a nonlinear acoustic metamaterial beam considering third harmonic generation *New J. Phys.* **20** 123028
- [32] Bae M H and Oh J H 2020 Amplitude-induced bandgap: new type of bandgap for nonlinear elastic metamaterials *J. Mech. Phys. Solids* **139** 103930
- [33] Settini V, Lepidi M and Bacigalupo A 2021 Nonlinear dispersion properties of one-dimensional mechanical metamaterials with inertia amplification *Int. J. Mech. Sci.* **201** 106461
- [34] Gong C, Fang X and Cheng L 2022 Band degeneration and evolution in nonlinear triatomic metamaterials *Nonlinear Dyn.* **111** 97–112
- [35] Nassar H, Yousefzadeh B, Fleury R, Ruzzene M, Alù A, Daraio C, Norris A N, Huang G and Haberman M R 2020 Nonreciprocity in acoustic and elastic materials *Nat. Rev. Mater.* **5** 667–85
- [36] Grinberg I, Vakakis A F and Gendelman O V 2018 Acoustic diode: wave non-reciprocity in nonlinearly coupled waveguides *Wave Motion* **83** 49–66
- [37] Wei L, Wang Y and Wang Y 2020 Nonreciprocal transmission of nonlinear elastic wave metamaterials by incremental harmonic balance method *Int. J. Mech. Sci.* **173** 105433
- [38] Fang X, Wen J, Cheng L and Li B 2021 Bidirectional elastic diode with frequency-preserved nonreciprocity *Phys. Rev. Appl.* **15** 54022
- [39] Fang X, Wen J, Benisty H and Yu D 2020 Ultrabroad acoustical limiting in nonlinear metamaterials due to adaptive-broadening band-gap effect *Phys. Rev. B* **101** 104304
- [40] Grinberg I and Matlack K H 2020 Nonlinear elastic wave propagation in a phononic material with periodic solid–solid contact interface *Wave Motion* **93** 102466
- [41] Jeon G J and Oh J H 2021 Nonlinear acoustic metamaterial for efficient frequency down-conversion *Phys. Rev. E* **103** 12212
- [42] Patil G U and Matlack K H 2021 Wave self-interactions in continuum phononic materials with periodic contact nonlinearity *Wave Motion* **105** 102763
- [43] Fang X, Wen J, Bonello B, Yin J and Yu D 2017 Ultra-low and ultra-broad-band nonlinear acoustic metamaterials *Nat. Commun.* **8** 1288
- [44] Yu M, Fang X and Yu D 2021 Combinational design of linear and nonlinear elastic metamaterials *Int. J. Mech. Sci.* **199** 106422
- [45] Sheng P, Fang X, Dai L, Yu D and Wen J 2023 Synthetical vibration reduction of the nonlinear acoustic metamaterial honeycomb sandwich plate *Mech. Syst. Signal Process.* **185** 109774
- [46] Detroux T, Renson L, Masset L and Kerschen G 2015 The harmonic balance method for bifurcation analysis of large-scale nonlinear mechanical systems *Comput. Meth. Appl. Mech. Eng.* **296** 18–38
- [47] Fang X, Wen J, Bonello B, Yin J and Yu D 2017 Wave propagation in one-dimensional nonlinear acoustic metamaterials *New J. Phys.* **19** 053007